Insights into hyperbolic phonon polaritons in *h*-BN using Raman scattering from encapsulated transition metal dichalcogenide layers

Jacob J. S. Viner [1], Liam P. McDonnell,[1] Pasqual Rivera,[2] Xiaodong Xu,[2] and David C. Smith[1,*]

[1]*School of Physics and Astronomy, University of Southampton, Southampton SO17 1BJ, United Kingdom*
[2]*Department of Physics, University of Washington, Seattle, Washington 98195, USA*

Alternative techniques for probing hyperbolic phonon polaritons (HPPs) in two-dimensional materials will support the development of the emerging technologies in this field. Previous reports have shown that it is possible for WSe$_2$ monolayers in contact with the hexagonal boron nitride (*h*-BN) to generate HPPs in the *h*-BN via Raman scattering. In this paper, we set out our results on HPP Raman scattering induced in *h*-BN by WSe$_2$ and MoSe$_2$ monolayers including multiple resonances at which the Raman scattering is enhanced. Analysis of the observed Raman line shapes demonstrates that Raman scattering allows HPPs with wave vectors with magnitudes significantly in excess of $15\,000\,\mathrm{cm}^{-1}$ to be probed. We present evidence that the Raman scattering can probe HPPs with frequencies less than the expected lower bound on the reststrahlen band, suggesting new HPP physics still waits to be discovered.

I. INTRODUCTION

The unique properties of hyperbolic phonon polaritons (HPPs) [1–4] are leading to their exploitation in a range of important applications [5,6], for instance, in the production of a new class of midinfrared (MIR) sources [7] which, while thermally excited, produce radiation which is narrow band [8] and spatially coherent [9,10]. Work on related sources indicates that it should be possible to combine these properties with high modulation frequencies, up to 10 MHz [11]. Another field in which HPPs are being exploited is MIR integrated nanophotonics for applications in surface-enhanced infrared spectroscopy [12] as well as subdiffraction imaging [6,13]. A recent highlight in this field has been the creation of reconfigurable waveguides and lenses for hyperbolic phonon polaritons [14,15] using phase change materials. Hyperbolic phonon polaritons allow subwavelength volume confinement [6,16,17] of midinfrared radiation by as much as a factor of 86. This confinement is not only being exploited for miniaturization but also allows the concentration of electromagnetic energy, allowing for strong coupling [18,19] and nonlinear effects [20–22]. By analogy with plasmonics, which are more lossy than HPPs [23], an even wider range of HPP applications, e.g., biosensors [24] and improving signal to noise photodetectors [7,8], is likely to emerge soon.

The two main techniques used to study HPPS are Fourier transform infrared (FTIR) spectroscopy [25] and scattering-type scanning near-field optical microscopy (s-SNOM) [26–28]. FTIR is simpler; however, it either requires specially prepared microfabricated structures [5] or prism coupling [5,29] to access the large wave vector HPP. The former is not suitable for probing HPPs in devices and the latter limits the wave vector that can be accessed.

s-SNOM [26–28] allows HPPs to be imaged in real space with impressive resolution and thus allows access to wave vectors of the order of ∼1000 times the free space wave vector [27,28]. However, this technique is complex and requires physical contact with the sample.

A HPP measurement method based upon the conversion of MIR to visible radiation would enable a wide range of new opportunities. The relative maturity of visible photonics means that such a method is likely to be much simpler. It should allow high-resolution (0.5 μm) imaging without the need for a near-field probe and because many of the key HPPs are wide band gap materials it should allow imaging of subsurface HPPs. Due to the much shorter wavelength of visible light such a method might allow access to even larger wave vector HPPs. Actually, it has already been shown that transition metal dichalcogenide (TMD) layers allow the probing of HPPs via Raman scattering of visible radiation [30–32]. However, no one has explored what information about HPPs can be obtained from the Raman spectra. In this paper we present significant results on HPP Raman scattering in TMDs. These include multiple resonances at which the HPP Raman features are enhanced in WSe$_2$ monolayers and measurements of HPP Raman features in Mo-based TMDs. Based upon these results we discuss the mechanism for HPP Raman scattering, the fact that it can access much higher wave vector HPPs than IR based techniques, and what Raman scattering of HPPs might bring to the field of HPP technologies.

II. MAIN BODY

Figure 1(a) shows a Raman spectrum of the encapsulated WSe$_2$ monolayer taken with an excitation energy of 1.866 eV. The observed Raman features can be separated into one-phonon peaks [$E''_{\mathrm{TO}}(M)$ at $196\,\mathrm{cm}^{-1}$; $E''_{\mathrm{TO}}(K)$ at $209\,\mathrm{cm}^{-1}$; $E'_{\mathrm{TO}}(M)$ at $229\,\mathrm{cm}^{-1}$; $E'(\Gamma)/A'_1(\Gamma)$ at $250\,\mathrm{cm}^{-1}$; $A''_2(M)/E'_{\mathrm{LO}}(K)$ at $258\,\mathrm{cm}^{-1}$) and two-phonon peaks (range
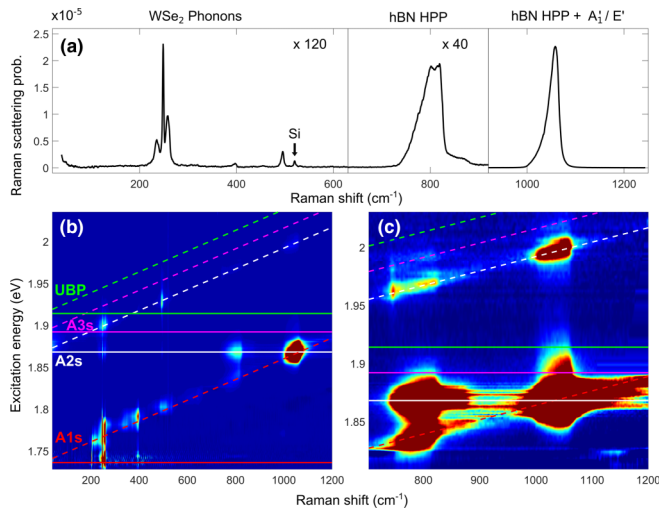
*D.C.Smith@soton.ac.uk

FIG. 1. (a) An individual Raman spectrum from the h-BN encapsulated WSe$_2$ sample with an excitation energy of 1.866 eV. The first two parts of the spectrum are scaled by factors of 120 and 40 for visibility. (b), (c) show color maps of the resonance behavior of the 800 and 1050 cm^{-1} h-BN Raman features; (b) presents the full spectral width including lower Raman shift features from the WSe$_2$ phonons, such as the strong 250 cm^{-1} $A_1'(\Gamma)/E'(\Gamma)$ peak, as well as the higher shift h-BN modes. (c) Presents a zoom of the higher shift part of the spectra presented in (b) with the colors adjusted to show a narrower range of intensities. The color indicates the intensity of the Raman scattering in logarithmic scale, with blue corresponding to lowest and red to highest intensity. The energies of the incoming and outgoing Raman resonances (solid and dashed lines) associated with the $A1s$, $A2s$, and $A3s$ excitonic states are shown with red, white, and pink lines, respectively. The green lines correspond to the resonance conditions for the lowest energy unbound electron-hole pair (UBP). The signal around 1.87 eV between the 800 and 1050 cm^{-1} peaks and shifts above 1100 cm^{-1} are from photoluminescence from the $A1s$ exciton, which follows the $A1s$ outgoing resonance.

of shifts up to 500 cm^{-1}) and two features at around 730–850 cm^{-1} and 1000–1080 cm^{-1}. Further discussion of the WSe$_2$ phonon Raman peaks and their attribution can be found in the literature [31,33–36]. The 730–850 cm^{-1} and 1000–1080 cm^{-1} features have previously been associated with scattering of excitons in the monolayer by a h-BN HPP (lower shift feature) and a combination of a h-BN HPP and a monolayer A_1' phonon (upper shift feature). This hypothesis is strongly supported by the facts that no Raman scattering is observed at comparable Raman shifts [31,32] in samples where WSe$_2$ monolayers are not in intimate contact with h-BN, and the only peak observed in the Raman spectra of h-BN [30,32,37] is at 1380 cm^{-1}. The peaks at smaller Raman shifts, which only involve phonons, are characteristically narrower with widths of the order of 0.25 meV (2 cm^{-1}), whereas the HPP related features are significantly broader, at 10 meV (80 cm^{-1}). The Raman features can also be observed in Figs. 1(b) and 1(c) where we present color maps of the resonance Raman spectra of an encapsulated WSe$_2$ monolayer. All the features show clear resonance behavior in the color maps. For instance, the Raman peak at 250 cm^{-1}, assigned to the degenerate A_1'/E' phonons [35,38], has four resonances, when

the incoming and scattered photons are resonant with the $A1s$ and $A2s$ bright excitonic states. As previously reported, the 730–850 cm^{-1} feature shows a clear outgoing resonance with the $A1s$ state and incoming resonance with the $A2s$ state [31,32]. As also previously reported, the 1000–1080 cm^{-1} feature shows a strong resonance at ∼1.865 eV which is both an outgoing resonance with the $A1s$ and an incoming resonance with the $A2s$, i.e., a double resonance. In addition, the same features have at least two other resonances at higher laser energies which have not been reported before. The clearest of these is an outgoing resonance associated with the $A2s$ exciton. There is also a weaker resonance, approximately 20 meV higher in energy corresponding to the $A3s$ exciton. As more clearly shown in Fig. 1(b), the features at the outgoing resonances show a characteristic behavior in which the higher shift scattering is resonant at higher laser energies. This is particularly visible from 1.95 to 2 eV. This is clear proof that the two broad features, with Raman shifts centered at approximately 800 and 1050 cm^{-1}, can be associated with a band of excitations rather than a single underlying excitation.

In order to better understand the resonance behavior and to determine the energy of the excitonic states involved, resonance profiles of the Raman scattering were determined for the two features as presented in Fig. 2. As each feature is associated with a band of excitations, the extracted resonance profile changes at different Raman shifts across the feature. For both of these h-BN features, three resonance profiles were determined, each by integrating the Raman scattering for a 5 cm^{-1} band around a center Raman shift. This process is described in the Supplemental Material, Sec. S1 [39]. The resonance profiles presented in Fig. 2 clearly show the $A1s$ outgoing and $A2s$ incoming resonances previously observed [30–32], as well as the higher energy resonances we observed. Interestingly there is no statistically significant Raman scattering associated with the h-BN related features at the $A1s$ incoming resonance. However, the significant additional noise due to the strong $A1s$ luminescence means the upper limit on any scattering at these laser energies is comparable with the strength of the Raman scattering at the highest energy resonances. In the case of the 730–850 cm^{-1} feature, shown in Fig. 2(a), the $A1s$ outgoing resonance near 1.83 eV shifts to lower energy, as expected, for the lower center Raman shifts. The two higher energy resonances above 1.95 eV show the same behavior indicating they are also both outgoing resonances. For the 1000–1080 cm^{-1} feature profiles shown in Fig. 2(b), the $A1s$ outgoing and $A2s$ incoming resonances fall at the same energy, creating a double resonance with the measured Raman scattering two orders of magnitude greater than that of the Raman feature at 730–850 cm^{-1}.

The resonance profiles were all fitted using the standard third-order perturbation theory prediction for Raman scattering [39] that assumes that the exciton-phonon scattering occurs in a single step. In order to fit all of the resonances, the model requires a minimum of three excitonic states. Unfortunately, this requires six exciton-phonon scattering matrix elements. This makes getting a unique fit for these parameters impossible. However, the energy and lifetime parameters for the three excitons obtained from the six independent resonance profiles, with and without setting some of the scattering matrix elements to zero, were remarkably consistent
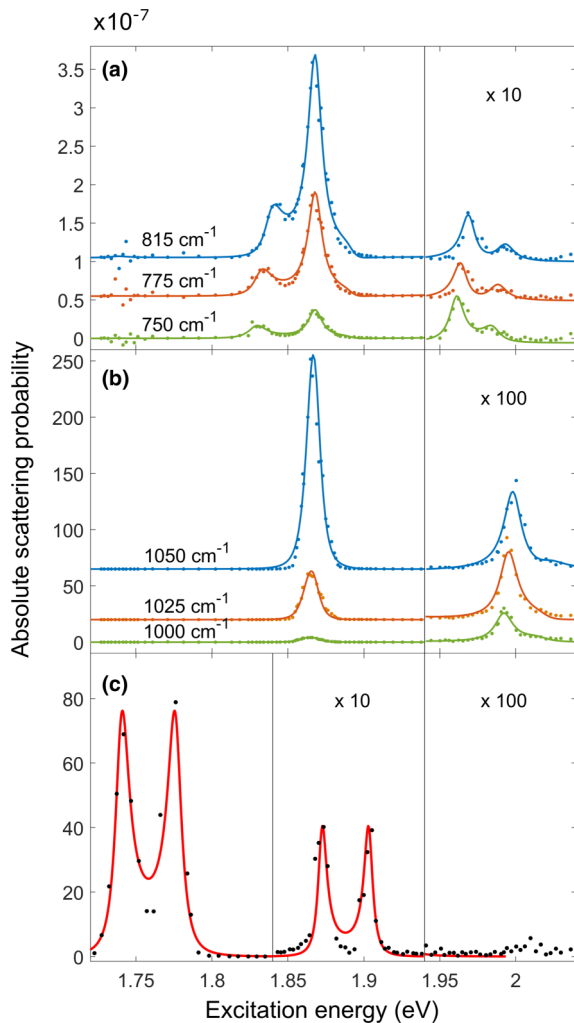
FIG. 2. Resonance profiles for the (a) 800 cm^{-1} or (b) 1050 cm^{-1} h-BN Raman features determined at different Raman shifts within the feature. The insets present vertically scaled subsections of the 815 and 1050 cm^{-1} resonance profiles. Peaks in the resonance profile observed in this range are associated with the $A2s$ and $A3s$ outgoing resonance conditions. The solid lines show fits to the resonance behavior using three-state, third-order, perturbation-theory resonant Raman scattering models where the three states are the $A1s$, $A2s$, and $A3s$ excitons in WSe$_2$. The resonances at $\sim$1.84 eV and between 1.95 and 2.0 eV are outgoing resonances and thus change energy with Raman shift. The resonance at $\sim$1.85 eV is the $A2s$ incoming resonance. The $A1s$ incoming resonance would fall around 1.74 eV but no statistically significant Raman signal is observed. The noise in the resonance data at the energy of the $A1s$ exciton is a photo-luminescence signal from the $A1s$ exciton and trion. (c) Resonance profiles of the WSe$_2$ 250 cm^{-1} single gamma point phonon over the same energy range. The left side of the plot shows the $A1s$ incoming and outgoing resonances. The right side shows the $A2s$ resonance with intensity scaled up by a factor of 20.

as shown in the Supplemental Material, Sec. S2 [39] (see, also, Refs. [40–42] therein). These fits give the energy (with fit estimated errors) for the three excitonic states to be 1.735 ± 0.002, 1.867 ± 0.001, and 1.892 ± 0.005. The first two energies are to within experimental error the same as the $A1s$ and $A2s$ energies obtained from fits to reflectivity spectra [43] and separate fits to the A'_1 phonon's resonance profiles shown
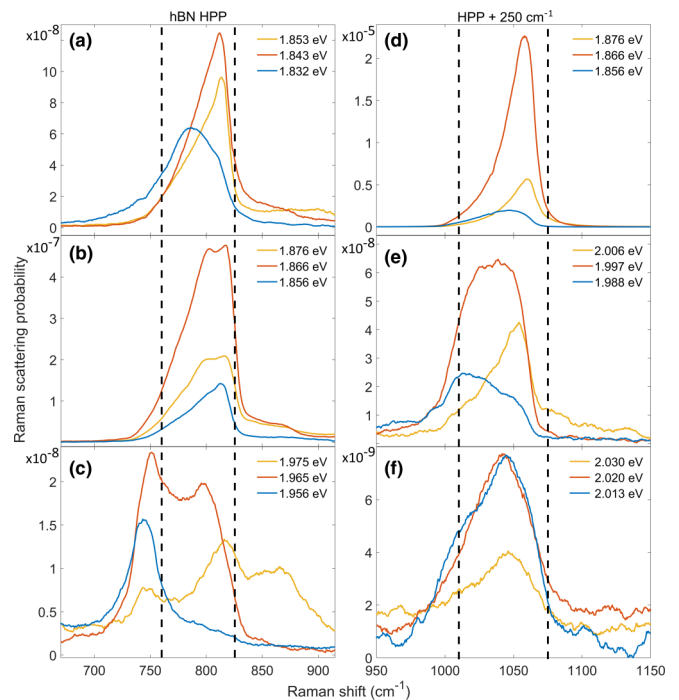
FIG. 3. Raman spectra showing the line shapes of the 800 (a), (c) and 1050 cm^{-1} (d)–(f) h-BN associated Raman peaks at various resonances. The orange curve shows the spectrum at the peak of the specified resonance and the blue and yellow curves show spectra taken at ±10 meV either side of the resonance. (a) $A1s$ outgoing, (b) $A2s$ incoming, (c) $A2s$ outgoing, (d) $A1s$ outgoing = $A2s$ incoming, (e) $A2s$ outgoing, and (f) $A3s$ outgoing. The lower shift peak observed in (c), in the 1.956 eV spectra, at about 750 cm^{-1}, is associated with a multiphonon peak rather than h-BN HPPs as can be seen more clearly in Fig. 1(c). This is only observed at the $A2s$ outgoing resonance. The agreement of the shift of this peak with three times the shift of the A'_1 peak suggests that it is due to emission of three A'_1 phonons.

in Fig. 2(c). The third energy is in agreement, to within a few meV, with previously published values for the $A3s$ excitonic state [44,45] as well as values obtained from reflectivity measurements of the sample [39]. This is an unusual report of a Raman resonance with the $A3s$ state.

Based upon the agreement between the measured energies of the first three excitonic energies and our model for the Rydberg series [46] we can predict the energy of the remaining excitonic states and the minimum energy unbound electron-hole states. As shown with green lines in Fig. 1, the threshold for excitation of unbound electron-hole states is less than the laser energy associated with the $A2s$ and $A3s$ outgoing resonances. Thus, it is possible that the initial optically excited state at these resonances is a real, unbound pair excitation rather than a virtual excitonic state.

One of the key characteristic features of the h-BN related Raman scattering is the broad line shapes. However, as shown in Fig. 3, the observed line shape depends on the resonance and the energy of the laser relative to the peak of the resonance. This is more obvious at the outgoing resonance but also true at the incoming resonances. The qualitative differences between the resonances can be rationalized as being due to the variation of the resonance conditions across the line shape and
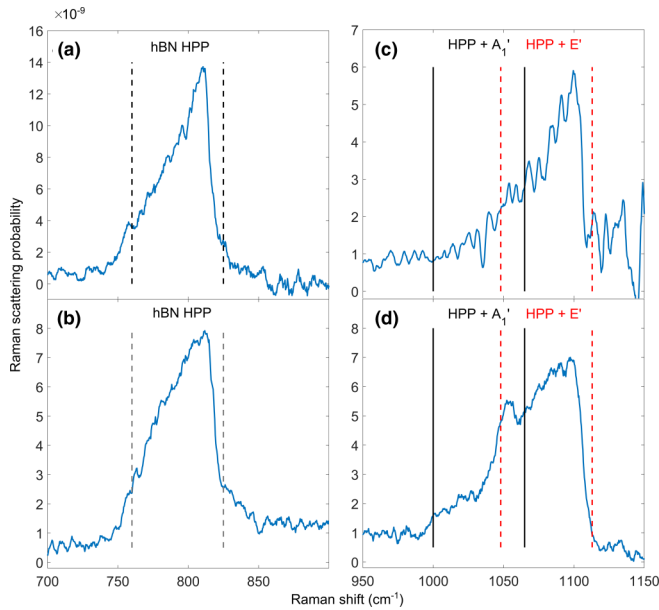
FIG. 4. Raman spectra of the *h*-BN encapsulated MoSe$_2$ mono-layer sample. Panels (a), (b) show the broad 800 cm^{-1} *h*-BN Raman peak with reststrahlen band shifts marked with dashed lines. Panels (c), (d) show the spectra around 1050 cm^{-1}, with markings at the reststrahlen band shifts plus the MoSe$_2$ $A_1'(\Gamma)$ phonon (240 cm^{-1}) in black, also plus the MoSe$_2$ $E'(\Gamma)$ phonon (288 cm^{-1}) in red. Panels (a,c) are from spectra taken around the $A1s$ outgoing/$A2s$ incoming resonances at 1.80 eV. Panels (b,d) are from spectra taken with the laser energy between the $B1s$ outgoing resonance and the $B2s$ incoming resonance at 2.01 eV.

how these depend on laser energy. For instance, the relative suppression of the higher Raman shift scattering at an out-going resonance for lower laser energies occurs because the lower shift scattering is closer to resonance with the outgoing state. However, attempts to quantitatively correct for this effect to obtain a single underlying line shape did not produce a consistent line shape independent of the laser energy. Despite this, it is possible to draw some general conclusions about the underlying line shape. In particular, for the 730–850 cm^{-1} feature the line shape covers the whole of the reststrahlen band. In fact, at the low shift side of the peak the line shape continues smoothly beyond the reststrahlen band. In general, the highest scattering is closer to the upper bound of the reststrahlen band; however, the exact form of the peak varies with the resonance. The line shape of the 1000–1080 cm^{-1} feature is very similar to the 730–850 cm^{-1} feature—in this case spanning, and at lower shifts extending beyond, the reststrahlen band shifted up by 250 cm^{-1} as would be expected if this feature was due to an emission of a combination of the HPPs responsible for the 730–850 cm^{-1} feature and the A_1'/E' phonon.

Having fully analyzed the data for the encapsulated WSe$_2$ we now turn our attention to the results for encapsulated MoSe$_2$. The strength of the *h*-BN related Raman peaks in encapsulated MoSe$_2$ is significantly weaker; see Fig 4. In MoSe$_2$, the features are observed only when the laser energy is tuned to the $A2s$ or $B2s$ excitons. In both cases, the resonances are near-double resonances with the $A1s$ and $B1s$ excitons, respectively; however, they are not fully doubly resonant. The

fact that in MoSe$_2$ the resonances are significantly further from double resonance compared to WSe$_2$ is likely to be the main reason why these features are so much weaker in MoSe$_2$. Due to the weak scattering, it was not possible to obtain clear spectra apart from at the peak of the resonance, or to fully analyze the resonance behavior. However, there is considerably more information available from the resonant spectra. In particular, the upper shift feature in MoSe$_2$ is considerably broader than the lower shift feature. As shown in Fig 4, it is possible to explain this if the upper shift feature is in fact due to a combination of a HPP and either an A_1' (lower Raman shifts) or E' phonon (higher Raman shifts). In the case of the WSe$_2$ these phonons are degenerate and so it is possible that the upper shift feature also involves a contribution from the E' phonon. In addition, and importantly, the line shape of the lower shift feature is very similar to the same feature in WSe$_2$ and in particular extends beyond the reststrahlen band at lower shifts. Thus, the observation of Raman scattering outside of the reststrahlen band is not a feature of a single material or sample, but is more general.

While the attribution of the *h*-BN features to HPPs is not new, so far few have tried to understand the line shape in terms of this model. To fully model the Raman line shape would require a model not only for the HPPs but also a model for TMD excitons and for the HPP-exciton interaction. However, it is reasonable to expect that the density of states of the HPP may well dominate the line shape. Therefore we have used a T-matrix model, developed by Passler and Paarmann [47], to predict the IR absorption spectrum of HPPs for our structure, measured in an Otto configuration experiment, as a function of an in-plane wave vector of the absorbed light. The absorption spectrum predictions were made using the *h*-BN dielectric function determined by Caldwell *et al.* [16] and layer thicknesses constrained by atomic force microscopy and fitting to the optical reflectivity spectra. The predicted spectra were fitted to extract the dispersion relation for the HPP, i.e., the energy of the HPP as a function of an in-plane wave vector. For some in-plane wave vectors it is possible to observe multiple, different energy HPPs which have different mode profiles in the direction normal to the plane. As shown in Fig. 5(a) as the in-plane wave vector increases, the number of possible modes increases and the energy of a specific mode decreases. In a Raman scattering momentum conservation should apply to the wave vector of the incoming photon and the sum of the wave vectors of the outgoing phonon and HPPs generated during the scattering process. This places a limit on the maximum wave vector HPPs that can be generated by Raman scattering comparable to the wave number of visible light, $\sim 15\,000$ cm^{-1}. If we use the wavelength of light resonant with the $A2s$ exciton in WSe$_2$, then based upon backscattering of radiation incident at 30°, reasonable for our objective lens, we predict that the maximum wave vector HPPs we should generate in momentum conserving Raman scattering would have a magnitude of 15 050 cm^{-1}. As shown in Fig. 5 HPPs with wave vectors with magnitude are restricted to the energy range 800–820 cm^{-1}, which is clearly too small a range to explain the observed Raman feature which extends below 750 cm^{-1}. Defects and other effects can lead to nonmomentum conserving Raman scattering. As shown in Fig. 4, if we assume the maximum wave vector of HPPs observed in Ra-
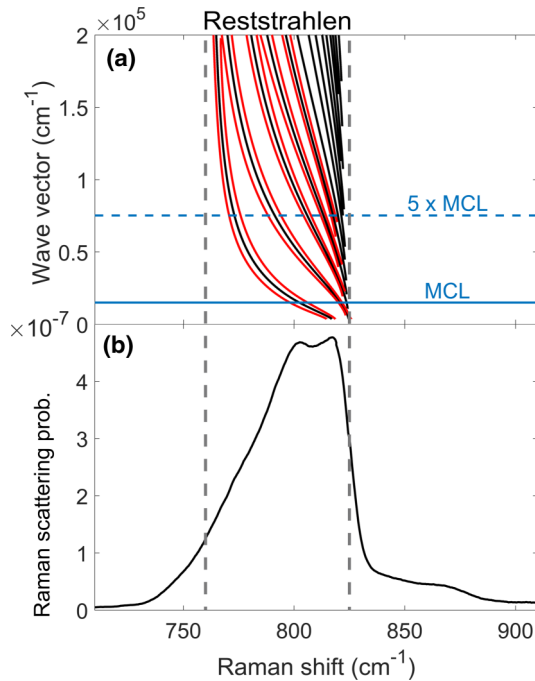
FIG. 5. (a) Dispersion relation for the hyperbolic phonon polariton modes, determined using the 4×4 transfer matrix approach of Passler and Paarmann [47]. The black lines show the bands of allowed modes and the red lines indicate their widths (at half magnitude) for the first five allowed HPP modes. The maximum in-plane momentum available in a single phonon Raman process based on the incident angle of the beam from the 0.5 NA objective is $15\,050\,\text{cm}^{-1}$ at the $A2s$ energy. This momentum conserving limit is marked with a solid blue line labeled MCL. Five times this limit is also marked with a dashed blue line. (b) shows a Raman spectrum taken on the h-BN encapsulated WSe$_2$ monolayer sample with an excitation energy of 1.866 eV, on resonance with the WSe$_2$ $A2s$ exciton. The h-BN TO and LO frequencies of 760 and $825\,\text{cm}^{-1}$ are marked with dashed vertical lines, between which is the reststrahlen band.

man scattering is five times that of the momentum conserving limit the range of the HPP Raman feature would be predicted to increase significantly to $760–820\,\text{cm}^{-1}$. Therefore, it is difficult to believe that Raman scattering does not probe HPPs with wave vectors significantly bigger than the momentum conserving limit of $15\,050\,\text{cm}^{-1}$. However, even if we place no upper limit on the wave vectors of the HPP which can be detected by Raman scattering, the range of the feature the theory predicts is narrower than the range observed in Raman scattering measurements. Fundamentally, it is not possible for the current model to produce scattering below the lower reststrahlen band edge. Thus, while it is highly likely that HPPS are responsible for the two features associated with them in Raman spectra of h-BN encapsulated TMD layers the simple HPP model set out above cannot explain the width of these features.

We now need to consider why the simple HPP model fails and what additional physics is required to explain the observed Raman features. An obvious possibility is that we have used the incorrect parameters for the rreststrahlen band. However, a review of the literature gives multiple independent measurements of these parameters based on IR spectroscopy

[16,37,48,49], and while there are variations in the extracted parameters, none of the measurements supports the lower bound of the reststrahlen band being below $760\,\text{cm}^{-1}$. Another alternative is that the $730–850\,\text{cm}^{-1}$ feature is a combination peak involving absorption of a thermal phonon. However, the measurements were performed at 4 K and the thermal energy, which corresponds to $\sim 3\,\text{cm}^{-1}$, is insufficient to significantly extend the feature to lower shifts. Another possibility is that at very large wave vectors the ZO phonon responsible for the HPP disperses to lower energy. However, there is no obvious mechanism allowing us to couple to such a large wave vector HPP. Thus, currently we do not have a good explanation of the width of the two Raman features associated with HPPs in these structures. While it is possible that the resolution of this issue is associated with the TMD layers, it is also possible that the ability of Raman scattering to access large wave vector HPPs is allowing us to access unique HPP effects not yet understood.

The results set out in this paper add considerably to our knowledge about the h-BN HPP Raman features observed previously in h-BN encapsulated WSe$_2$ structures. In addition to the h-BN Raman scattering previously reported at the WSe$_2$ $A1s$ outgoing and $A2s$ incoming resonances, we have observed h-BN associated Raman scattering at outgoing resonances of the $A2s$ and $A3s$ excitonic states. In MoSe$_2$, we have also observed h-BN HPP features. In this material, they are associated with double resonances with the incoming photons resonant with the $A2s$ or $B2s$ excitons and the outgoing photons resonant with the $A1s$ or $B1s$ excitons respectively. From the MoSe$_2$ spectra, we can deduce that in this material the upper HPP feature involves emission of a HPP and either an A_1' or E' phonon, with both cases contributing to the overall line shape. It is quite likely that this is also true for WSe$_2$ but the degeneracy of the phonons in this material makes this difficult to confirm.

However, the most important outcomes of this study are associated with the HPP. Firstly, it is clear that compared to IR reflectivity measurements, resonance Raman scattering allows access to a much greater range of HPPs with larger wave vectors. Even momentum conserving Raman scattering allows access to wave vectors a factor of 10 greater than accessible by IR measurements, and there is good evidence that Raman scattering is not momentum conserving, allowing even larger wave vector modes to be studied. In addition, there is a mystery as to how Raman scattering can occur at Raman shifts below the lower bound on the reststrahlen band determined from IR measurements. The solution to this mystery may give us insights into HPPs that cannot be achieved via other techniques. The insights need not be restricted to HPPs associated with the layers of h-BN. It is possible to transfer exfoliated TMD flakes onto a wide range of substrates. This suggests they could make an ideal probe for HPPS associated with a wide range of materials and metamaterials. This paper shows that doing this will give insight into HPPs in these structures that is difficult to achieve in other ways.

III. METHODS

The h-BN encapsulated monolayer MoSe$_2$ and WSe$_2$ samples were fabricated by hot pickup using a dry polycarbonate

on a polydimethylsiloxane (PDMS) stamp from individual mechanically exfoliated monolayers [50]. The WSe$_2$ sample was encased within a h-BN layer, top 36 nm, and bottom 27 nm, thick. The bottom h-BN layer was on top of a 20 nm graphite layer which sat atop a 300 nm thick SiO$_2$ coated Si wafer. The MoSe$_2$ sample followed the same structure, with top and bottom h-BN thicknesses of 30 and 20 nm, respectively, and a 4 nm graphite thickness. These are the same samples that feature in a larger resonance Raman study [43,51] with the same experimental setup. The measurements presented here were performed with the sample under vacuum at 4 K in a helium flow cryostat. A Coherent Mira 900 Ti:sapphire laser in cw mode and a Coherent CR-599 cw dye laser were used to excite the samples in backscattering geometry via a 50×0.5 NA long working distance microscope objective. This allowed Raman spectra to be taken with excitation energies from 1.60 to 2.24 eV. The incident power on the sample was 100 μW. The Raman spectra were measured with a TriVista 555 spectrometer with the first two stages of the spectrometer set in subtractive mode and a liquid nitrogen cooled charge-coupled device (CCD).

Linear polarizers were placed in the exciting laser beam before the sample and in between the sample and spectrometer. For each excitation energy, Raman spectra were taken with these polarizers set collinear and with them crossed. The crossed polarizer spectra were subtracted from the collinear spectra which had the effect of removing the photoluminescence (PL) signal while preserving the Raman signal. At energies where the PL signal in the spectrum was many orders of magnitude greater than the Raman signal, such as near the $A1s$ exciton energy, residual PL was present after subtraction.

The Raman signal from the SiO$_2$ coated Si substrate was used to calibrate the Raman spectra for frequency. The intensity of the Si peak was used with Si resonance Raman data from the literature [52] to convert the data to absolute scattering probability. A transfer matrix model of the stack of layers in the samples was used to correct for the effect of thin film interference on the Raman intensity. The details of these corrections are given in the Supplemental Material of our previous paper [43].

IV. SUPPLEMENTAL MATERIAL

The Supplemental Material [39] contains discussion of the h-BN modes in a h-BN encapsulated MoSe$_2$ monolayer sample, including a resonance Raman color map and resonance profile of the 800 cm^{-1} mode. Reflectivity spectra are also discussed for the MoSe$_2$ and WSe$_2$ samples, with exciton energies extracted from those spectra presented with comparative literature values from [44,53–56]. Additional detail on the extraction and fitting of resonance profiles from the Raman spectra is also provided.

The data presented in this paper are openly available from the University of Southampton Repository [57].

[1] Z. Jacob, Nanophotonics: Hyperbolic phonon-polaritons, Nat. Mater. **13**, 1081 (2014).

[2] E. Yoxall, M. Schnell, A. Y. Nikitin, O. Txoperena, A. Woessner, M. B. Lundeberg, F. Casanova, L. E. Hueso, F. H. L. Koppens, and R. Hillenbrand, Direct observation of ultraslow hyperbolic polariton propagation with negative phase velocity, Nat. Photonics **9**, 674 (2015).

[3] T. Low, A. Chaves, J. D. Caldwell, A. Kumar, N. X. Fang, P. Avouris, T. F. Heinz, F. Guinea, L. Martin-Moreno, and F. Koppens, Polaritons in layered two-dimensional materials, Nat. Mater. **16**, 182 (2017).

[4] D. N. Basov, M. M. Fogler, and F. J. García De Abajo, Polaritons in van der Waals materials, Science **354**, aag1992 (2016).

[5] T. G. Folland, L. Nordin, D. Wasserman, and J. D. Caldwell, Probing polaritons in the mid- to far-infrared, J. Appl. Phys. **125**, 191102 (2019).

[6] P. Li, M. Lewin, A. V. Kretinin, J. D. Caldwell, K. S. Novoselov, T. Taniguchi, K. Watanabe, F. Gaussmann, and T. Taubner, Hyperbolic phonon-polaritons in boron nitride for near-field optical imaging and focusing, Nat. Commun. **6**, 7507 (2015).

[7] A. C. Jones and M. B. Raschke, Thermal infrared near-field spectroscopy, Nano Lett. **12**, 1475 (2012).

[8] G. Lu, J. R. Nolen, T. G. Folland, M. J. Tadjer, D. G. Walker, and J. D. Caldwell, Narrowband polaritonic thermal emitters driven by waste heat, ACS Omega **5**, 10900 (2020).

[9] R. Carminati and J. J. Greffet, Near-Field Effects in Spatial Coherence of Thermal Sources, Phys. Rev. Lett. **82**, 1660 (1999).

[10] J. J. Greffet, R. Carminati, K. Joulain, J. P. Mulet, S. Mainguy, and Y. Chen, Coherent emission of light by thermal sources, Nature (London) **416**, 61 (2002).

[11] L. Wojszvzyk, A. Nguyen, A.-L. Coutrot, M. Besbes, J.-P. Hugonin, B. Vest, and J.-J. Greffet, Fast modulation and polarization control of infrared emission by incandescent metasurfaces, in *Plasmonics: Design, Materials, Fabrication, Characterization, and Applications XVIII*, edited by T. Tanaka and D. P. Tsai (SPIE, Bellingham, WA, 2020).

[12] M. Autore, P. Li, I. Dolado, F. J. Alfaro-Mozaz, R. Esteban, A. Atxabal, F. Casanova, L. E. Hueso, P. Alonso-González, J. Aizpurua, A. Y. Nikitin, S. Vélez, and R. Hillenbrand, Boron nitride nanoresonators for phonon-enhanced molecular vibrational spectroscopy at the strong coupling limit, Light Sci. Appl. **7**, 17172 (2018).

[13] S. Dai, Q. Ma, T. Andersen, A. S. McLeod, Z. Fei, M. K. Liu, M. Wagner, K. Watanabe, T. Taniguchi, M. Thiemens, F. Keilmann, P. Jarillo-Herrero, M. M. Fogler, and D. N. Basov, Subdiffractional focusing and guiding of polaritonic rays in a natural hyperbolic material, Nat. Commun. **6**, 6963 (2015).

[14] K. Chaudhary, M. Tamagnone, X. Yin, C. M. Spägele, S. L. Oscurato, J. Li, C. Persch, R. Li, N. A. Rubin, L. A. Jauregui, K. Watanabe, T. Taniguchi, P. Kim, M. Wuttig, J. H. Edgar, A. Ambrosio, and F. Capasso, Polariton nanophotonics using phase-change materials, Nat. Commun. **10**, 4487 (2019).

[15] T. G. Folland, A. Fali, S. T. White, J. R. Matson, S. Liu, N. A. Aghamiri, J. H. Edgar, R. F. Haglund, Y. Abate, and J. D. Caldwell, Reconfigurable infrared hyperbolic metasurfaces using phase change materials, Nat. Commun. **9**, 4371 (2018).

[16] J. D. Caldwell, A. V. Kretinin, Y. Chen, V. Giannini, M. M. Fogler, Y. Francescato, C. T. Ellis, J. G. Tischler, C. R. Woods, A. J. Giles, M. Hong, K. Watanabe, T. Taniguchi, S. A. Maier, and K. S. Novoselov, Sub-diffractional volume-confined polaritons in the natural hyperbolic material hexagonal boron nitride, Nat. Commun. **5**, 5221 (2014).

[17] I. H. Lee, M. He, X. Zhang, Y. Luo, S. Liu, J. H. Edgar, K. Wang, P. Avouris, T. Low, J. D. Caldwell, and S. H. Oh, Image polaritons in boron nitride for extreme polariton confinement with low losses, Nat. Commun. **11**, 3649 (2020).

[18] C. R. Gubbin, R. Berte, M. A. Meeker, A. J. Giles, C. T. Ellis, J. G. Tischler, V. D. Wheeler, S. A. Maier, J. D. Caldwell, and S. De Liberato, Hybrid longitudinal-transverse phonon polaritons, Nat. Commun. **10**, 1682 (2019).

[19] N. C. Passler, C. R. Gubbin, T. G. Folland, I. Razdolski, D. S. Katzer, D. F. Storm, M. Wolf, S. De Liberato, J. D. Caldwell, and A. Paarmann, Strong coupling of epsilon-near-zero phonon polaritons in polar dielectric heterostructures, Nano Lett. **18**, 4285 (2018).

[20] A. Paarmann, I. Razdolski, A. Melnikov, S. Gewinner, W. Schöllkopf, and M. Wolf, Second harmonic generation spectroscopy in the reststrahlen band of SiC using an infrared free-electron laser, Appl. Phys. Lett. **107**, 081101 (2015).

[21] I. Razdolski, Y. Chen, A. J. Giles, S. Gewinner, W. Schöllkopf, M. Hong, M. Wolf, V. Giannini, J. D. Caldwell, S. A. Maier, and A. Paarmann, Resonant enhancement of second-harmonic generation in the mid-infrared using localized surface phonon polaritons in subdiffractional nanostructures, Nano Lett. **16**, 6954 (2016).

[22] N. C. Passler, I. Razdolski, S. Gewinner, W. Schöllkopf, M. Wolf, and A. Paarmann, Second-harmonic generation from critically coupled surface phonon polaritons, ACS Photonics **4**, 1048 (2017).

[23] J. D. Caldwell, O. J. Glembocki, Y. Francescato, N. Sharac, V. Giannini, F. J. Bezares, J. P. Long, J. C. Owrutsky, I. Vurgaftman, J. G. Tischler, V. D. Wheeler, N. D. Bassim, L. M. Shirey, R. Kasica, and S. A. Maier, Low-loss, extreme subdiffraction photon confinement via silicon carbide localized surface phonon polariton resonators, Nano Lett. **13**, 3690 (2013).

[24] D. Rodrigo, O. Limaj, D. Janner, D. Etezadi, F. J. García De Abajo, V. Pruneri, and H. Altug, Mid-infrared plasmonic biosensing with graphene, Science **349**, 165 (2015).

[25] A. J. Giles, S. Dai, I. Vurgaftman, T. Hoffman, S. Liu, L. Lindsay, C. T. Ellis, N. Assefa, I. Chatzakis, T. L. Reinecke, J. G. Tischler, M. M. Fogler, J. H. Edgar, D. N. Basov, and J. D. Caldwell, Ultralow-loss polaritons in isotopically pure boron nitride, Nat. Mater. **17**, 134 (2018).

[26] S. Dai, Z. Fei, Q. Ma, A. S. Rodin, M. Wagner, A. S. McLeod, M. K. Liu, W. Gannett, W. Regan, K. Watanabe, T. Taniguchi, M. Thiemens, G. Dominguez, A. H. Castro Neto, A. Zettl, F. Keilmann, P. Jarillo-Herrero, M. M. Fogler, and D. N. Basov, Tunable phonon polaritons in atomically thin van der Waals crystals of boron nitride, Science **343**, 1125 (2014).

[27] Z. Fei, A. S. Rodin, G. O. Andreev, W. Bao, A. S. McLeod, M. Wagner, L. M. Zhang, Z. Zhao, M. Thiemens, G. Dominguez, M. M. Fogler, A. H. Castro Neto, C. N. Lau, F. Keilmann, and D. N. Basov, Gate-tuning of graphene plasmons revealed by infrared nano-imaging, Nature (London) **487**, 82 (2012).

[28] J. Chen, M. Badioli, P. Alonso-González, S. Thongrattanasiri, F. Huth, J. Osmond, M. Spasenović, A. Centeno, A. Pesquera, P. Godignon, A. Zurutuza Elorza, N. Camara, F. J. García, R. Hillenbrand, and F. H. L. Koppens, Optical nano-imaging of gate-tunable graphene plasmons, Nature (London) **487**, 77 (2012).

[29] T. G. Folland, T. W. W. Ma, J. R. Matson, J. R. Nolen, S. Liu, K. Watanabe, T. Taniguchi, J. H. Edgar, T. Taubner, and J. D. Caldwell, Probing hyperbolic polaritons using infrared attenuated total reflectance micro-spectroscopy, MRS Commun. **8**, 1418 (2018).

[30] L. Du, Y. Zhao, Z. Jia, M. Liao, Q. Wang, X. Guo, Z. Shi, R. Yang, K. Watanabe, T. Taniguchi, J. Xiang, D. Shi, Q. Dai, Z. Sun, and G. Zhang, Strong and tunable interlayer coupling of infrared-active phonons to excitons in van der Waals heterostructures, Phys. Rev. B **99**, 205410 (2019).

[31] C. M. Chow, H. Yu, A. M. Jones, J. Yan, D. G. Mandrus, T. Taniguchi, K. Watanabe, W. Yao, and X. Xu, Unusual exciton-phonon interactions at van der Waals engineered interfaces, Nano Lett. **17**, 1194 (2017).

[32] C. Jin, J. Kim, J. Suh, Z. Shi, B. Chen, X. Fan, M. Kam, K. Watanabe, T. Taniguchi, S. Tongay, A. Zettl, J. Wu, and F. Wang, Interlayer electron–phonon coupling in WSe$_2$/hBN heterostructures, Nat. Phys. **13**, 127 (2016).

[33] H. Terrones, E. Del Corro, S. Feng, J. M. Poumirol, D. Rhodes, D. Smirnov, N. R. Pradhan, Z. Lin, M. A. T. Nguyen, A. L. Elías, T. E. Mallouk, L. Balicas, M. A. Pimenta, and M. Terrones, New first order Raman-active modes in few layered transition metal dichalcogenides, Sci. Rep. **4**, 4215 (2014).

[34] X. Zhang, X.-F. Qiao, W. Shi, J.-B. Wu, D.-S. Jiang, and P.-H. Tan, Phonon and Raman scattering of two-dimensional transition metal dichalcogenides from monolayer, multilayer to bulk material, Chem. Soc. Rev. **44**, 2757 (2015).

[35] S. Y. Chen, C. Zheng, M. S. Fuhrer, and J. Yan, Helicity-resolved Raman scattering of MoS$_2$, MoSe$_2$, WS$_2$, and WSe$_2$ atomic layers, Nano Lett. **15**, 2526 (2015).

[36] L. Du, M. Liao, J. Tang, Q. Zhang, H. Yu, R. Yang, K. Watanabe, T. Taniguchi, D. Shi, Q. Zhang, and G. Zhang, Strongly enhanced exciton-phonon coupling in two-dimensional WSe$_2$, Phys. Rev. B **97**, 235145 (2018).

[37] R. Geick, C. H. Perry, and G. Rupprecht, Normal modes in hexagonal boron nitride, Phys. Rev. **146**, 543 (1966).

[38] W. Zhao, Z. Ghorannevis, K. K. Amara, J. R. Pang, M. Toh, X. Zhang, C. Kloc, P. H. Tan, and G. Eda, Lattice dynamics in mono- and few-layer sheets of WS_2 and WSe_2, Nanoscale **5**, 9677 (2013).

[39] See Supplemental Material at http://link.aps.org/supplemental/10.1103/PhysRevB.104.165404 for and reflectivity and h-BN resonance Raman measurements.

[40] I. Bilgin, A. S. Raeliarijaona, M. C. Lucking, S. C. Hodge, A. D. Mohite, A. De Luna Bugallo, H. Terrones, and S. Kar, Resonant Raman and exciton coupling in high-quality single crystals of atomically thin molybdenum diselenide grown by vapor-phase chalcogenization, ACS Nano **12**, 740 (2018).

[41] D. Nam, J. U. Lee, and H. Cheong, Excitation energy dependent Raman spectrum of $MoSe_2$, Sci. Rep. **5**, 17113 (2015).

[42] P. Soubelet, A. E. Bruchhausen, A. Fainstein, K. Nogajewski, and C. Faugeras, Resonance effects in the Raman scattering of monolayer and few-layer $MoSe_2$, Phys. Rev. B **93**, 155407 (2016).

[43] L. P. McDonnell, J. Viner, P. Rivera, X. Xu, and D. C. Smith, Observation of intravalley phonon scattering of $2s$ excitons in $MoSe_2$ and WSe_2 monolayers, 2D Mater. **7**, 045008 (2020).

[44] M. Manca, M. M. Glazov, C. Robert, F. Cadiz, T. Taniguchi, K. Watanabe, E. Courtade, T. Amand, P. Renucci, X. Marie, G. Wang, and B. Urbaszek, Enabling valley selective exciton scattering in monolayer WSe_2 through upconversion, Nat. Commun. **8**, 14927 (2017).

[45] S. Y. Chen, Z. Lu, T. Goldstein, J. Tong, A. Chaves, J. Kunstmann, L. S. R. Cavalcante, T. Woźniak, G. Seifert, D. R. Reichman, T. Taniguchi, K. Watanabe, D. Smirnov, and J. Yan, Luminescent emission of excited Rydberg excitons from monolayer WSe_2, Nano Lett. **19**, 2464 (2019).

[46] J. J. S. Viner, L. P. McDonnell, D. A. Ruiz-Tijerina, P. Rivera, X. Xu, V. I. Fal'Ko, and D. C. Smith, Excited Rydberg states in $MoSe_2$/WSe_2 heterostructures, 2D Mater. **8**, 035047 (2021).

[47] N. C. Passler and A. Paarmann, Generalized 4×4 matrix formalism for light propagation in anisotropic stratified media:

Study of surface phonon polaritons in polar dielectric heterostructures, J. Opt. Soc. Am. B **34**, 2128 (2017).

[48] S. V. Ordin, B. N. Sharupin, and M. I. Fedorov, Normal lattice vibrations and the crystal structure of anisotropic modifications of boron nitride, Semiconductors **32**, 924 (1998).

[49] E. Franke, M. Schubert, H. Neumann, T. E. Tiwald, D. W. Thompson, J. A. Woollam, J. Hahn, and F. Richter, Phase and microstructure investigations of boron nitride thin films by spectroscopic ellipsometry in the visible and infrared spectral range, J. Appl. Phys. **82**, 2906 (1997).

[50] P. J. Zomer, M. H. D. Guimarães, J. C. Brant, N. Tombros, and B. J. Van Wees, Fast pick up technique for high quality heterostructures of bilayer graphene and hexagonal boron nitride, Appl. Phys. Lett. **105**, 013101 (2014).

[51] L. P. McDonnell, J. J. S. Viner, D. A. Ruiz-Tijerina, P. Rivera, X. Xu, V. I. Fal'ko, and D. C. Smith, Superposition of intra- and inter-layer excitons in twistronic $MoSe_2$/WSe_2 bilayers probed by resonant Raman scattering, 2D Mater. **8**, 035009 (2021).

[52] R. L. Aggarwal, L. W. Farrar, S. K. Saikin, A. Aspuru-Guzik, M. Stopa, and D. L. Polla, Measurement of the absolute Raman cross section of the optical phonon in silicon, Solid State Commun. **151**, 553 (2011).

[53] J. Horng, T. Stroucken, L. Zhang, E. Y. Paik, H. Deng, and S. W. Koch, Observation of interlayer excitons in $MoSe_2$ single crystals, Phys. Rev. B **97**, 241404(R) (2018).

[54] A. Arora, K. Nogajewski, M. Molas, M. Koperski, and M. Potemski, Exciton band structure in layered $MoSe_2$: From a monolayer to the bulk limit, Nanoscale **7**, 20769 (2015).

[55] E. Liu, J. van Baren, T. Taniguchi, K. Watanabe, Y.-C. Chang, and C. H. Lui, Magnetophotoluminescence of exciton Rydberg states in monolayer WSe_2, Phys. Rev. B **99**, 205420 (2019).

[56] A. Arora, J. Marcus, K. Nogajewski, M. Koperski, C. Faugeras, M. Potemski, K. Nogajewski, J. Marcus, C. Faugeras, and M. Potemski, Excitonic resonances in thin films of WSe_2: From monolayer to bulk material, Nanoscale **7**, 10421 (2015).

[57] J. Viner, L. Mcdonnell, and D. Smith, "Data to Support Insights into HPPs in hBN via TMD Raman" (2021), doi: 10.5258/SOTON/D1734.